

# 1 Development of a global ~90 m water body map

## 2 using multi-temporal Landsat images

3 Dai Yamazaki

4 Department of Integrated Climate Change Projection Research,  
5 Japan Agency for Marine-Earth Science and Technology  
6 3173-25, Showa-machi, Kanazawa-ku, Yokohama, Kanagawa, 236-0001, Japan  
7 +81-45-778-5565  
8 d-yamazaki@jamstec.go.jp

9 Mark A. Trigg

10 Willis Research Fellow, School of Geographical Sciences, University of Bristol  
11 University Road, Clifton, Bristol, BS8 1SS, UK  
12 Mark.Trigg@bristol.ac.uk

13 Daiki Ikeshima

14 Department of Civil Engineering, Tokyo Institute of Technology  
15 2-12-1-M1-6 O-okayama, Meguro-ku, Tokyo 152-8552, Japan  
16 ikeshima.d.aa@m.titech.ac.jp

## 17 **Abstract**

18 This paper describes the development of a Global 3 arc-second Water Body Map (G3WBM),  
19 using an automated algorithm to process multi-temporal Landsat images from the Global Land  
20 Survey (GLS) database. We used 33,890 scenes from 4 GLS epochs in order to delineate a  
21 seamless water body map, without cloud and ice/snow gaps. Permanent water bodies were  
22 distinguished from temporal water-covered areas by calculating the frequency of water body  
23 existence from overlapping, multi-temporal, Landsat scenes. By analyzing the frequency of  
24 water body existence at 3 arc-second resolution, the G3WBM separates river channels and  
25 floodplains more clearly than previous studies. This suggests that the use of multi-temporal  
26 images is as important as analysis at a higher resolution for global water body mapping. The  
27 global totals of delineated permanent water body area and temporal water-covered area are 3.25  
28 and 0.49 million km<sup>2</sup> respectively, which highlights the importance of river-floodplain  
29 separation using multi-temporal images. The accuracy of the water body classification was

30 validated in Hokkaido (Japan) and in the contiguous United States using an existing water body  
31 databases. There was almost no commission error, and about 70% of lakes  $>1 \text{ km}^2$  shows  
32 relative water area error  $<25\%$ . Though smaller water bodies ( $<1 \text{ km}^2$ ) were underestimated  
33 mainly due to omission of shoreline pixels, the overall accuracy of the G3WBM should be  
34 adequate for larger scale research in hydrology, biogeochemistry, and climate systems and  
35 importantly includes a quantification of the temporal nature of global water bodies.

## 36 **Keywords**

37 Landsat GLS, water body mapping, global analysis, river, floodplain

## 38 **1. Introduction**

### 39 **1.1 Background**

40 Terrestrial water in rivers and lakes is essential for both human beings and ecosystems (Oki  
41 and Kanae, 2006). River and lakes affect the climate system via land-atmosphere interaction  
42 processes such as carbon burial and  $\text{CO}_2$  exchange as well as other biogeochemical processes  
43 (Cole et al., 2007; Sjögersten et al., 2014). Delineating the spatial and temporal distribution of  
44 rivers and lakes is important for understanding the water, energy and carbon cycles, both at  
45 local and global scales (Downing et al., 2012, 2014; Allen et al., 2015). Mapping water bodies  
46 at a global scale is therefore a fundamental step to understand the role of inland water bodies in  
47 climate systems (Palmer et al., 2015).

48 Until very recently, globally available water body maps have been limited in resolution, but  
49 in parallel with recent computational advances in various research fields, a high-resolution,  
50 high-accuracy global water body database is required. For example, global-scale water body  
51 maps have been used in river width calculation for hydrodynamic modeling (O'Loughlin et al.,  
52 2013; Yamazaki et al., 2014a and 2014b; Sampson et al., 2015). In addition, given that

53 biogeochemical processes in small lakes may be more active than large lakes (Downing, 2010),  
54 a higher-resolution database is needed to accurately quantify the global carbon cycle.

55 Many global-scale water body databases have been developed in recent years (see Table 1).  
56 The SRTM Water Body Data (SWBD) (NASA/NGA, 2003) accurately captures water bodies at  
57 1 arc-second resolution (about ~30 m at the Equator), but it does not cover the entire globe.  
58 Some large rivers in SWBD are disconnected by observational gaps which significantly reduce  
59 channel connectivity and therefore the utility of the database for hydrology studies. The Global  
60 Land Cover Facility (GLCF) MODerate resolution Imaging Spectroradiometer (MODIS) 250 m  
61 water mask (Carroll et al., 2009) has a global coverage, but the 250 m resolution is not adequate  
62 to resolve small channels or lakes. The GLCF MODIS water mask is considered to be a  
63 “snapshot” of circa-2000, so the temporal change in water bodies (such as potential inundation  
64 of floodplains) is not represented. Recently, using Landsat images globally, Feng et al. (2015)  
65 developed the GLCF Inland surface Water data (GIW) at 30 m resolution and Verpoeter et al.  
66 (2014) developed Global Water Body data (GLOWABO) at 0.5 arc-second resolution. However,  
67 the temporal change of water bodies was not considered in previous high-resolution water body  
68 databases.

69 Some water body databases do consider temporal change in water extent. The Global Lake  
70 and Wetland Database (GLWD) (Lehner and Döll, 2004) used a classification of surface water  
71 types (e.g. river, lake, floodplain, wetland) and depicts the global distribution of each surface  
72 water type at ~1 km resolution. Prigent et al. (2007) and Papa et al. (2010) developed a 25 km  
73 resolution inundated area map (Global Inundation Extent from Multi-Satellite: GIEMS) with  
74 monthly temporal variations, though the 25-km resolution is not sufficient to depict individual  
75 rivers or lakes. Fluet-Chouinard et al. (2015) downscaled GIEMS to a 15 arc-second resolution.  
76 The downscaled product (GIEMS-D15) quantifies global water extent at mean annual minimum,  
77 mean annual maximum and long term maximum.

78 **Table 1. Comparison of global surface water database**

Product	Resolution	Coverage	Frequency of Water	Reference
SWBD	1 sec (~30 m)	N60-S54	No	NASA/NGA, 2003
GLCF MODIS	7.5 sec (~250 m)	N90-S90	No	Carroll et al., 2009
GLCF GIW	30 m	N81-S81	No	Feng et al., 2015
GLOWABO	0.5 sec (~15m)	N81-S56	No	Verpoeter et al., 2014
GLWD	30 sec (~1 km)	N90-S60	Water type classification	Lehner and Doll, 2004
GIEMS	25 km (equal area)	N90-S90	Monthly flood extent	Papa et al., 2010
GIEMS-D15	15 sec (~500 m)	N90-S60 <sup>a</sup>	Mean annual max/min	Fluet-Couinard et al., 2015
G3WBM	3 sec (~90 m)	N81-S60	Multi-scene analysis	This Study

79 <sup>a</sup> Greenland is not included

80 A major problem in delineating a high-accuracy, high-resolution, water body map comes  
 81 from the fact that water extent can change in time and space. Given that rivers, lakes,  
 82 floodplains and wetlands show different characteristics in hydrodynamics, ecosystems and  
 83 biogeochemistry, it is obviously better to separate permanent water bodies (e.g. low water river  
 84 channels, lakes with permanent water coverage) and temporal water-covered areas (e.g.  
 85 floodplains, wetlands, paddy fields) in water body mapping. For example, accurate delineation  
 86 of low-water river channels (excluding floodplains) is important for improving flood forecasting  
 87 by global-scale river models (e.g. Pappenburger et al., 2012), and information on temporal  
 88 dynamics of surface waters is valuable to estimate global wetland carbon inventory (e.g.  
 89 Bridgham et al., 2013). Multi-temporal images are needed to carry out frequency analysis, but  
 90 this significantly increases the quantity of data to be handled, especially when analysis is done  
 91 at a high resolution. Due to this difficulty in data handling and processing, previous  
 92 high-resolution water maps do not consider temporal change of water extent, and frequency of  
 93 water body existence is only represented in low resolution databases.

## 94 **1.2 Objective**

95 The objective of this study is to develop a new high-resolution global water body map with  
 96 information on the frequency of water body existence. An automated algorithm was developed

97 to handle multi-temporal Landsat images at a global scale and to analyze the frequency of water  
98 body existence at 3 arc-second resolution (about 90 m at the equator). The algorithm was also  
99 designed to exclude observational gaps caused by cloud or ice/snow covers by compositing  
100 multiple satellite images. The Global 3 arc-second Water Body Map (G3WBM) was generated  
101 by applying the developed algorithm to Landsat images in the GLCF Global Land Survey  
102 (GLS) database (Gutman et al., 2013). The main aim is to generate a global permanent water  
103 body map (e.g. low water river channels, lakes with permanent water coverage) at 3 arc-second  
104 resolution, but as a consequence of defining the permanent water areas, additional information  
105 on temporal water-covered areas (e.g. floodplains, paddy fields) is included in the G3WBM.

## 106 **2. Data**

### 107 **2.1 Landsat GLS database**

108 As a starting point for the water body map delineation, we used the GLCF Landsat Global  
109 Land Survey (GLS) database (Gutman et al., 2013). The GLS database attempts to provide one  
110 cloudless image acquired at each location in World Reference System (WRS). One set of  
111 global-coverage images is prepared for 5 different epochs (i.e. GLS1975, GLS1990, GLS2000,  
112 GLS2005 and GLS2010). The GLS1975 consists of Landsat Multi-Spectral Scanner (MSS)  
113 images, while the other epoch collections are based on Landsat TM (Thematic Mapper) and  
114 ETM+ (Enhanced Thematic Mapper Plus) images. Landsat images with lesser cloud cover were  
115 selected for the GLS database, but they are not always perfectly cloud-free. Landsat GLS  
116 images can be downloaded freely from the GLCF website (<http://glcf.umd.edu/data/gls/>).

117 We used all TM and ETM+ images from the Landsat GLS database. A total of 33,890 scenes  
118 were used; 7,375 from GLS1990, 8,756 from GLS2000, 9,365 from GLS2005, and 8,484 from  
119 GLS2010. The water body map was calculated by combining information from 4 spectral bands  
120 and one thermal band; Band 2 (green: G), Band 3 (red: R), Band 4 (near infra-red: NIR), Band 5  
121 (short wave infra-red: SWIR), and Band 6 (thermal infra-red). Band 1 (blue: B) was also used to

122 generate RGB composites for the post-classification analysis and validation steps (see Sections  
123 4 and 5). Please note that there are overlapping areas between adjacent Landsat paths, so that the  
124 number of available observations can be larger than 4. The overlapping areas become wider at  
125 higher latitude, so that the number of observations is larger in higher latitude (even though  
126 eastern Siberia is missing by GLS1990).

## 127 **2.2 Digital Elevation Model**

128 A Digital Elevation Model (DEM) was used to generate an ocean mask and also for  
129 distinguishing shadows from water bodies. We used the global 3 arc-second DEM downloaded  
130 from the Viewfinder Panoramas webpage (<http://www.viewfinderpanoramas.org/dem3.html>).  
131 The Viewfinder Panoramas DEM (hereafter VFP-DEM) was generated mainly using the Shuttle  
132 Radar Topography Mission 3 arc-second DEM (SRTM3 DEM) (Farr et al., 2007) for regions  
133 below 60N, but for above 60N uses the GeoBase DEM for Canada, and Russian topography  
134 maps for the Eurasian continent. Large voids (i.e. blank areas due to no data, usually found over  
135 water bodies and in mountain areas) in the original SRTM3 DEM were carefully filled in by the  
136 developer of the VFP-DEM using auxiliary topography information such as printed topography  
137 maps. However, some small voids remain in the distributed DEM and we fill these remaining  
138 voids by interpolation using the inverse square distance weighted method.

139 An ocean mask was generated by marking 0 m elevation pixels which are connected to outer  
140 oceans (i.e. 0 m pixels in inland areas are excluded from the ocean mask). In order to include  
141 river pixels with 0 m elevation in the analysis, coastline data from OpenStreetMap (available  
142 online from <http://openstreetmapdata.com/data/coastlines>) was also used to generate the ocean  
143 mask. Pixels in the ocean mask were excluded from water body classification because Landsat  
144 GLS images often have large amount of clouds over oceans and we are only interested in  
145 terrestrial water bodies.

146 Elevation gradient was calculated from the VFP-DEM in order to distinguish shadows from  
147 water bodies. Elevation gradient (in meter per pixel) was calculated as the maximum elevation  
148 difference between each pixel and its 8 neighboring pixels. If a pixel is lower than any of its  
149 neighbors, the elevation gradient was set to 0 m.

## 150 **2.3 SWBD water mask**

151 The Shuttle Radar Topography Mission Water Body Data (SWBD) (NASA/NGA, 2003) was  
152 additionally used in order to ensure channel connectivity in the delineated water body map (See  
153 Section 3.5). The SWBD was a byproduct of the SRTM3 DEM which was generated by C-band  
154 radar interferometer. Because the coverage of SWBD is between 60N and 56S, connectivity  
155 correction was not performed above 60N.

## 156 **3. Method**

### 157 **3.1 Landsat image processing**

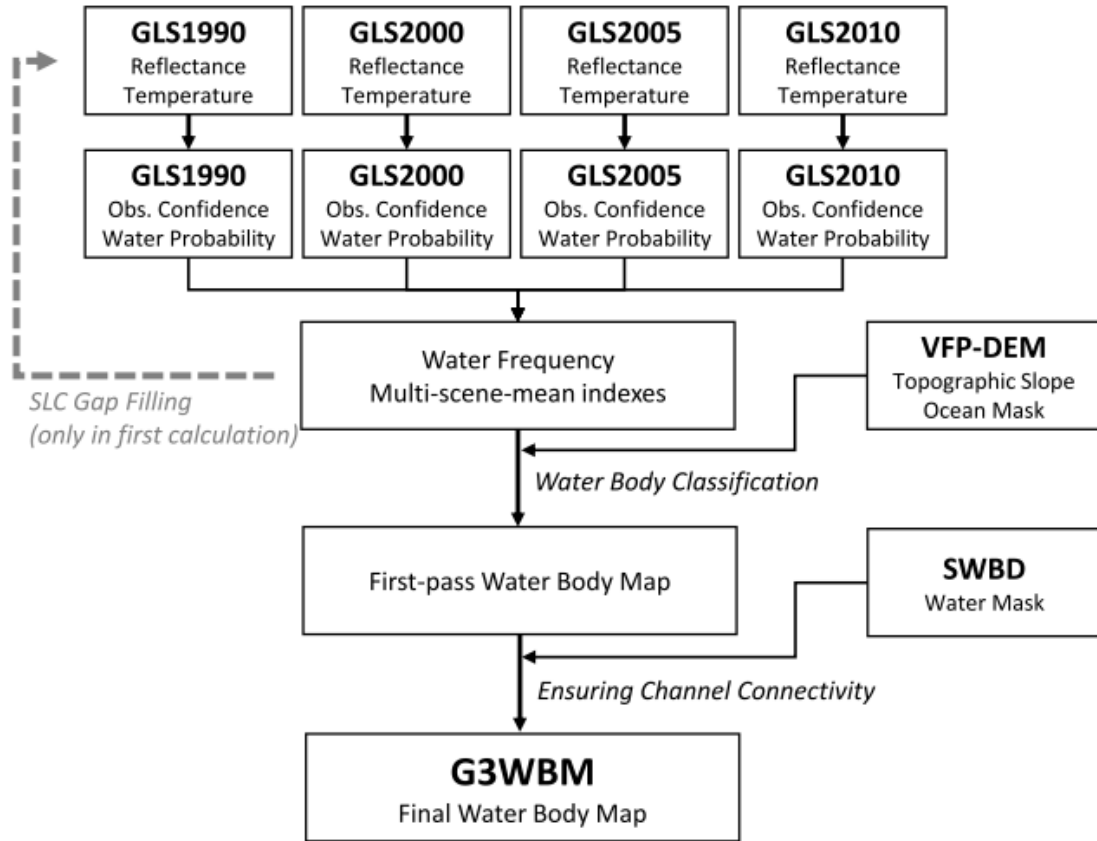
158 Each Landsat image was converted to 3 arc-sec resolution (about ~90 m at the Equator) in  
159 the WGS84 grid coordination system by nearest point resampling. Given that the georeferenced  
160 error of GLS images was approximately 25 m (Gutman et al., 2013), the georeferenced error  
161 should not be a problem at the 3 arc-second resolution. Then, top of the atmosphere reflectance  
162 and brightness temperature were calculated from the digital number (DN) using the conversion  
163 method described by Chander and Markham (2003) and Chander et al. (2009). Reflectance of  
164 blue band  $\rho_B$ , green band  $\rho_G$ , red band  $\rho_R$ , near infra-red band  $\rho_{NIR}$ , and short wave  
165 infra-red band  $\rho_{SWIR}$  were calculated from the DN of bands 1, 2, 3, 4, and 5, respectively.  
166 Brightness temperature  $Tb$  (in centigrade) was calculated from the DN of band 6. Then, the  
167 Normalized Difference Water Index (NDWI) and the Normalized Difference Vegetation Index  
168 (NDVI) were calculated as follows:

169 
$$NDWI = \frac{\rho_G - \rho_{SWIR}}{\rho_G + \rho_{SWIR}} \quad (1),$$

170 
$$NDVI = \frac{\rho_{NIR} - \rho_R}{\rho_{NIR} + \rho_R} \quad (2).$$

171 We selected the Modified Normalized Difference Water Index (MNDWI) proposed by Xu  
172 (2006) from the many variations of NDWI methods (e.g. McFeeters, 1996; Ji et al., 2009).  
173 Landsat-7 images after 31<sup>st</sup> May 2003 have striping gaps due to the failure of the Scan Line  
174 Corrector (SLC) (Maxwell et al. 2007). The SLC gaps were filled by the interpolation method  
175 described in Appendix A1. Note that the resolution conversion and grid coordination change  
176 were done with the “gdalwarp” function of Geospatial Data Abstraction Library (GDAL)  
177 (Warmerdam, 2008), while other steps were calculated using Fortran90 codes originally  
178 developed by the authors. A schematic diagram of the developed algorithm is shown in Figure  
179 1.





180

181 **Figure 1: Schematic diagram of the developed algorithm. Note that more than 4 images**  
 182 **are used where Landsat scenes are overlapped with adjacent scenes.**

### 183 3.2 Frequency of Water Body Existence

184 The index “water frequency” was introduced to separate permanent water bodies, temporal  
 185 water-covered areas, and land pixels. Water frequency  $Fw_i$  of pixel  $i$  was defined by the  
 186 equation (3):

$$187 \quad Fw_i = \frac{\sum_{j=1}^N (O_{i,j} W_{i,j})}{\sum_{j=1}^N O_{i,j}} \quad (3),$$

188 where  $O_{i,j}$  is observation confidence at pixel  $i$  in Landsat scene  $j$ ,  $W_{i,j}$  is water  
 189 probability at pixel  $i$  in Landsat scene  $j$ ,  $N$  is the total number of Landsat scenes available

190 at pixel  $i$ . Equation (3) means that water frequency is calculated by the observation-confidence  
 191 weighted average of water probability. Note that parameters in the following steps (e.g.  
 192 thresholds and constants in classification conditions) were mainly taken from previous studies  
 193 (e.g. Irish, 2000; Ji et al., 2009) but are adjusted by trial and error, based on validation.

194 **<Observation Confidence>**

195 Observation confidence  $O_{i,j}$  represents the certainty of judging land surface type at pixel  
 196  $i$  in Landsat scene  $j$ . Observation confidence is 1 when land is judged to be perfectly observed  
 197 without cloud or ice/snow cover, while it becomes smaller when land is not clearly observable  
 198 (a minimum value was set to 0.001). Observation confidence is defined by Equation (4):

$$199 \quad O_{i,j} = \max[1 - Pci, 0.001] \quad (4),$$

200 where  $Pci$  is a probability index of cloud/ice existence at pixel  $i$  in Landsat scene  $j$ . The  
 201 probability index  $Pci$  ranges from 0 (low cloud/ice probability) to 1 (high cloud/ice  
 202 probability), and is given by the equation (5):

$$203 \quad Pci = \frac{\min[\rho_{GRN}, 0.25]}{0.25} f_{NDLI} f_{Tb} \quad (5),$$

204 where  $\rho_{GRN}$  is minimum reflectance of green, red and near infra-red bands,  $f_{NDLI}$  is a  
 205 correction factor using Normalized Difference Land Index (NDLI, see Appendix A2) and  $f_{Tb}$   
 206 is a correction factor using brightness temperature. Given that cloud and ice/snow are highly  
 207 refractive in visible and near infra-red bands, the probability of cloud/ice existence can be  
 208 mainly judged by the minimum reflectance of the red, green and near infra-red bands  
 209 ( $\rho_{GRN} = \min[\rho_G, \rho_R, \rho_{NIR}]$ ). The correction factors  $f_{NDLI}$  and  $f_{Tb}$  were introduced to  
 210 separate cloud/ice and highly-reflective rock/vegetation. Detailed explanations on these  
 211 correction factors are outlined in Appendix A2.

212 **<Water probability>**

213 Water probability in Equation (3) was calculated using Equation (6):

$$214 \quad W_{i,j} = P_{NDWI} f_{NDVI} \quad (6),$$

215 where  $P_{NDWI}$  is a probability index using NDWI and  $f_{NDVI}$  is a correction factor using NDVI.

216 The probability index  $P_{NDWI}$  was given by the equation (7):

$$217 \quad P_{NDWI} = \begin{cases} 0 & (NDWI < 0) \\ NDWI / 0.3 & (0 \leq NDWI \leq 0.3) \\ 1 & (0.3 < NDWI) \end{cases} \quad (7).$$

218 When NDWI is larger than 0.3, the pixel is considered to be water and when smaller than 0, the  
219 pixel is considered to be land. For an NDWI between 0 and 0.3, the water body existence is  
220 represented by probability. Because shadows sometimes show high NDWI as water, the  
221 correlation function using NDVI  $f_{NDVI}$  was introduced to distinguish shadow and water. The  
222 detailed description of  $f_{NDVI}$  is summarized in Appendix A3.

### 223 **3.3 Multi-scene mean indexes**

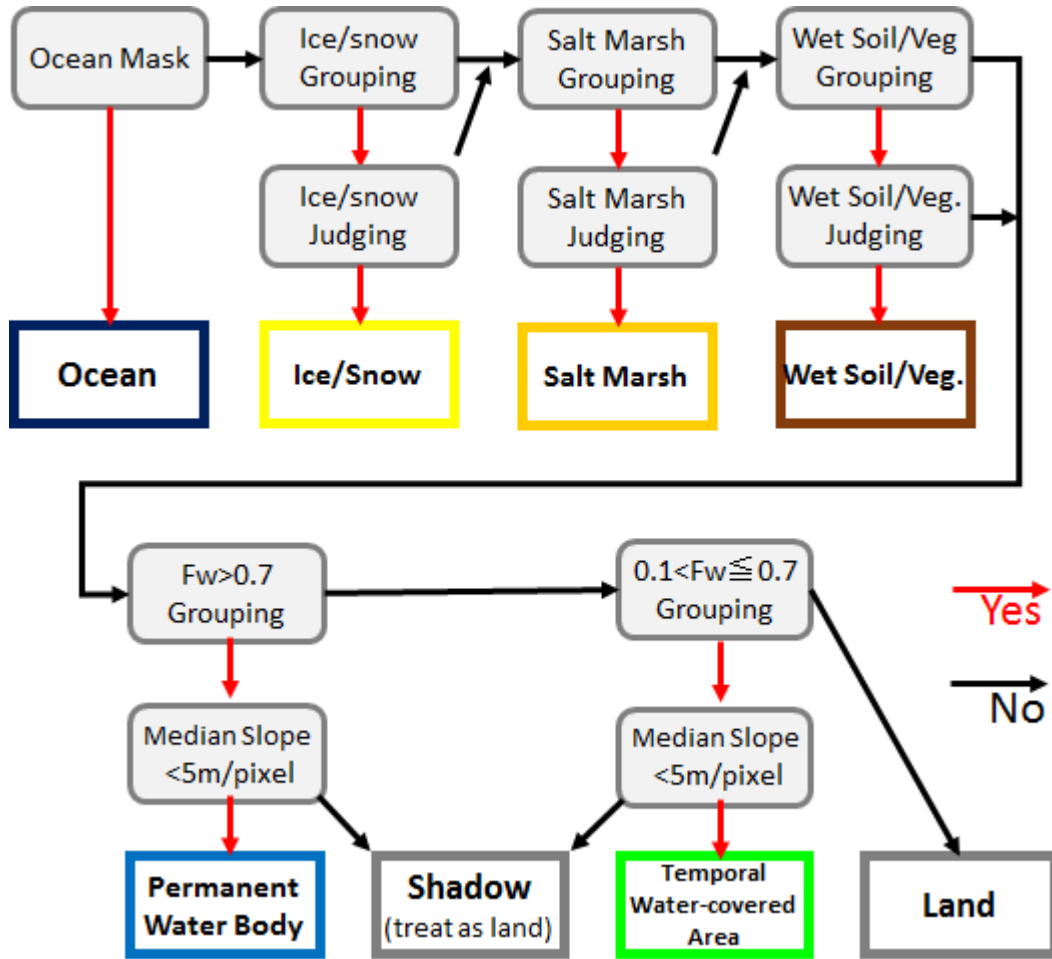
224 In addition to water frequency  $Fw_i$ , multi-scene mean indexes (i.e. reflectance, NDWI,  
225 NDVI, and brightness temperature) are calculated. These multi-scene mean indexes were used  
226 for water mask classification in the water body classification step (see Section 3.4). For each  
227 index  $V$  (e.g. reflectance, NDWI, NDVI), the multi-scene mean was defined by Equation (8):

$$228 \quad \bar{V}_i = \frac{\sum_{j=1}^N (O_{i,j} W_{i,j} V_{i,j})}{\sum_{j=1}^N (O_{i,j} W_{i,j})} \quad (8),$$

229 where  $\bar{V}_i$  is the multi-scene-mean of index  $V$  at pixel  $i$ .  $O_{i,j}$  is the observation  
230 confidence,  $W_{i,j}$  is the water probability,  $V_{i,j}$  is the target index, all at pixel  $i$  in Landsat  
231 scene  $j$ .  $N$  is the number of observation scenes available at pixel  $i$ . Multi-scene-mean  
232 indexes at pixel  $i$  are calculated for reflectance of each bands ( $\bar{\rho}_{Bi}$ ,  $\bar{\rho}_{Gi}$ ,  $\bar{\rho}_{Ri}$ ,  $\bar{\rho}_{NIRi}$ ,  
233  $\bar{\rho}_{SWIRi}$ ), minimum reflectance of green, red and near-infra-red bands ( $\bar{\rho}_{GRNi}$ ), NDWI, NDVI  
234 and brightness temperature ( $\bar{WI}_i, \bar{VI}_i, \bar{Tb}_i$ ).

### 235 **3.4 Water Body Classification**

236 The main aim of this study is to delineate a permanent water body map. For that purpose,  
237 water frequency was used to distinguish permanent water bodies from temporal water-covered  
238 areas. However, some land covers (e.g. ice, snow, salt marsh, wet soil, wet vegetation and  
239 shadow) show a high NDWI, thus they might mistakenly be classified as water (i.e. commission  
240 error). Therefore, other land cover types which showed similar characteristics to water, were  
241 excluded before classifying permanent water bodies and temporal water-covered areas. The  
242 flowchart of classification steps is shown in Figure 2.



243  
244 **Figure 2. Flowchart of classification steps**

245 **<Exclusion of high-NDWI non-water surface>**

246 Ice/snow, salt marsh, and wet soil/vegetation are excluded as high-NDWI non-water surface  
 247 using the criteria listed in Table 2. In order to avoid generation of a patchy land type  
 248 classification, adjacent pixels with similar characteristics were grouped using the grouping  
 249 criteria. Then, one classification type was assigned to pixels in each group by the judging  
 250 criteria. Group-mean index  $\bar{V}^g$  was calculated from multi-scene-mean index  $\bar{V}_i$  of pixels in  
 251 each group as follows:

252 
$$\bar{V}^g = \frac{\sum_{i=1}^M \bar{V}_i}{M} \quad (9),$$

253 where  $M$  is the number of pixels in each group. Note that the thresholds in Table 2 were  
 254 determined by trial and error, repeating water body classification and visual checking detailed in  
 255 Section 3.6.

256 **Table 2. Criteria used for high-NDWI non-water land classification.**

	Ice/snow	Salt marsh	Wet soil/vegetation
Grouping Criteria	$Fw_i > 0.3$ $\bar{\rho}_{GRN_i} > 0.15$ $\bar{Tb}_i < 2$ $\bar{WI}_i > 0.4$ $\bar{VI}_i > -0.2$	$Fw_i > 0.1$ $\bar{\rho}_{GRN_i} > 0.25$ $\bar{Tb}_i > 0$ $\bar{WI}_i > 0.4$ $\bar{VI}_i > -0.2$	$\bar{\rho}_{GRN_i} < 0.15$ $0.0 < \bar{WI}_i < 0.5$ $-0.15 < \bar{VI}_i < 0.3$
Judging Criteria	$\bar{\rho}_{GRN}^g > 0.2$ $\bar{Tb}^g < 0$ $\bar{WI}^g > 0.6$ $\bar{VI}^g > 0.2$	$\bar{\rho}_{GRN}^g > 0.35$	$\bar{WI}^g < 0.4$ $\bar{VI}^g > 0.05$

257

258 As ice and snow show a high NDWI similar to water, pixels with ice or snow cover were  
 259 excluded before water body classification. Adjacent pixels whose multi-scene-mean indexes  
 260 (water frequency  $Fw_i$ , minimum reflectance of green, red and near infra-red bands  $\bar{\rho}_{GRN_i}$ ,  
 261 brightness temperature  $\bar{Tb}_i$ , normalized water index  $\bar{WI}_i$  and normalized vegetation index  
 262  $\bar{VI}_i$ ) satisfy the grouping criteria for ice/snow in Table 2 were grouped as potential ice/snow  
 263 pixels. If group-mean indexes of the grouped pixels satisfy the judging criteria in Table 2,  
 264 potential ice/snow pixels within each group were judged to be true ice/snow class. Pixels which  
 265 were not classified as ice/snow were passed to salt marsh classification.

266 Salt marsh has a high reflectance in visible bands and has relatively low reflectance in the  
 267 short wave infra-red band. Therefore, salt marsh shows a high NDWI even when it is not  
 268 inundated. In order to distinguish dry salt marsh from true water bodies, pixels considered to  
 269 represent salt marsh were excluded before water mask classification using the grouping and

270 judging criteria in Table 2. Pixels which were not classified as salt marsh were passed to wet  
271 soil/vegetation classification.

272 Wet soil/vegetation sometimes shows a relatively high NDWI, even when the land surface is  
273 not inundated. In order to accurately delineate true water bodies, pixels which showed moderate  
274 NDWI and moderate NDVI were classified as wet soil/vegetation using the criteria in Table 2.  
275 Pixels which were not classified as wet soil/vegetation were passed to the following water body  
276 classification.

### 277 <Water Body Classification>

278 After excluding ice/snow, salt marsh, and wet soil/vegetation, the remaining pixels were  
279 classified as permanent water bodies, temporal water-covered areas and land, based on water  
280 frequency. However, pixels affected by shadows should be distinguished from water bodies  
281 because they sometimes show a high NDWI. Here, elevation gradient (calculated from the DEM,  
282 defined in Section 2.2) was used to distinguish water bodies from shadows. For permanent  
283 water body delineation, adjacent pixels which had  $Fw_i > 0.7$  were grouped. In order to  
284 exclude mountain shadows, the grouped pixels were classified as permanent water body when  
285 more than half the group's pixels had an elevation gradient smaller than 5 m per pixel (i.e.  
286 relatively flat areas). Otherwise they were classed as shadow. Remaining pixels were passed to  
287 temporal water-covered area classification.

288 Adjacent pixels with  $0.1 < Fw_i \leq 0.7$  were grouped. The grouped pixels were classified as  
289 temporal water-covered areas when the group-mean NDWI was larger than 0.5 and when more  
290 than half of the pixels had an elevation gradient smaller than 5 m per pixel. All remaining pixels  
291 were classified as land.

## 292 **3.5 Ensuring Channel Connectivity**

293 The proposed frequency analysis is based on the assumption that the river channel location is  
294 stable for long periods. Therefore, the developed algorithm is not applicable to river segments

295 where channel position frequently changes with time. In these cases, river channels may be  
296 classified as temporal water-covered areas when channel positions are different in different  
297 Landsat scenes. In order to ensure flow connectivity of river channels, we overlaid the SWBD  
298 water mask onto the delineated water body map. For minimizing the correction amount, we only  
299 used SWBD water bodies which were larger than 100 km. Excessive modification of small  
300 lakes could be avoided by using this size threshold, and the connectivity correction could be  
301 restricted to large rivers. Pixels which were not classified as permanent water but are treated as  
302 water bodies in the SWBD, were changed to permanent water body pixels. It is reported that the  
303 SWBD also has gaps within water bodies (Carroll et al., 2009), but this did not cause a  
304 connectivity problem in this study because we confirmed that locations of water body gaps were  
305 not overlapping between the SWBD and the GLS images.

### 306 **3.6 Visual Checking**

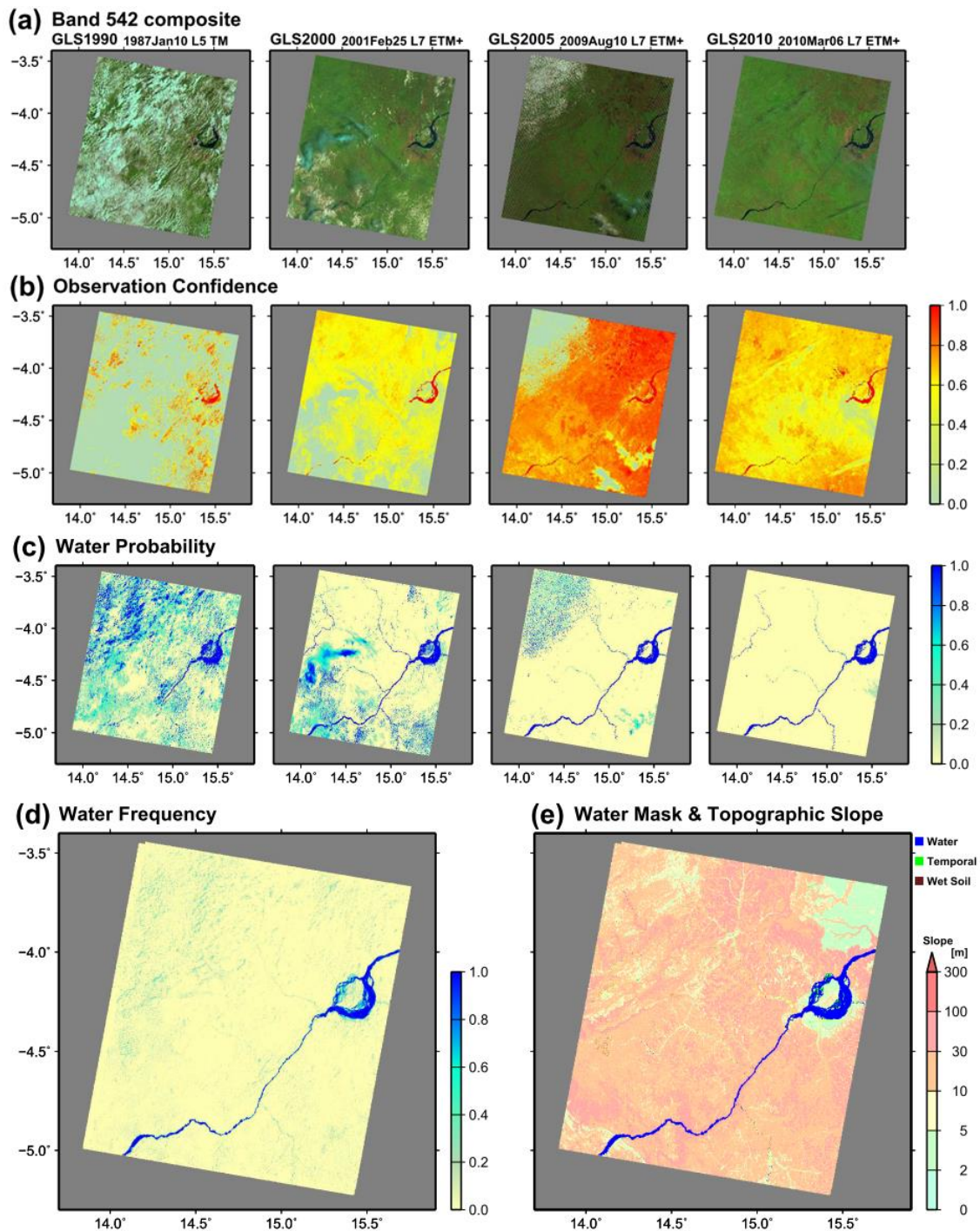
307 We generated a JPEG image of the developed water body map at each 5 degree tile, and  
308 visually examined every image to check whether the classifications were appropriate or not.  
309 Images were visually checked for consistency and continuity, as well as against other spatial  
310 data and images available, such as Google and Bing satellite images. If critical errors were  
311 found, we revised the coefficients and thresholds used in the classification step (e.g. numbers in  
312 Table 2) and recalculated the entire water body map globally. This visual checking iteration  
313 method was repeated more than 10 times until all major misclassifications were eliminated.  
314 While much of the processing and analytical testing described in the results section are  
315 automated, this human visual step was important for identifying some of the subtle anomalies  
316 that can occur when trying to apply an automated method globally using multi-temporal images.

## 317 **4. Results**

318 Firstly, we demonstrated how the proposed algorithm removes clouds and calculates water  
319 frequency. A part of the Congo River (Landsat World Reference System 2 path 182 row 086;



320 E13.7-E15.9, S5.3-S3.4) was selected as an example because cloudy images were included. The  
321 algorithm was applied to four images available at path 182 row 086 (the acquisition dates of the  
322 four images are shown in Figure 3). The band 5-4-2 composite image of each GLS scene are  
323 shown in Figure 3a. In the band 5-4-2 composite image, vegetation, rock, water, cloud water  
324 (warm cloud) and cloud ice (cold cloud) are colored with green, red, dark blue, white and pale  
325 blue, respectively. All images contain cloud water and/or cloud ice which disrupt the earth  
326 observation. The observation confidence calculated by Equation (4) is shown in Figure 3b.  
327 Locations of pixels with low observation confidence (grey) agree well with observable cloud  
328 locations. Water probability (Figure 3c) was high for pixels representing open waters. Some  
329 pixels under cloud showed a high probability, but their impact in water frequency calculation is  
330 low because their observation confidence is low. In the GLS1990 image, some pixels along the  
331 Congo mainstem showed a low water probability because of cloud cover. However, water  
332 frequency at these pixels was not reduced by the cloud cover because observation confidence  
333 was also low when pixels were covered by clouds. Figure 3d illustrates water frequency  
334 calculated from the four images. While river and land were clearly distinguished, water  
335 frequency was slightly high in some pixels with cloud cover. These pixels were successfully  
336 judged to be land after applying the classification algorithm (see Figure 3e).

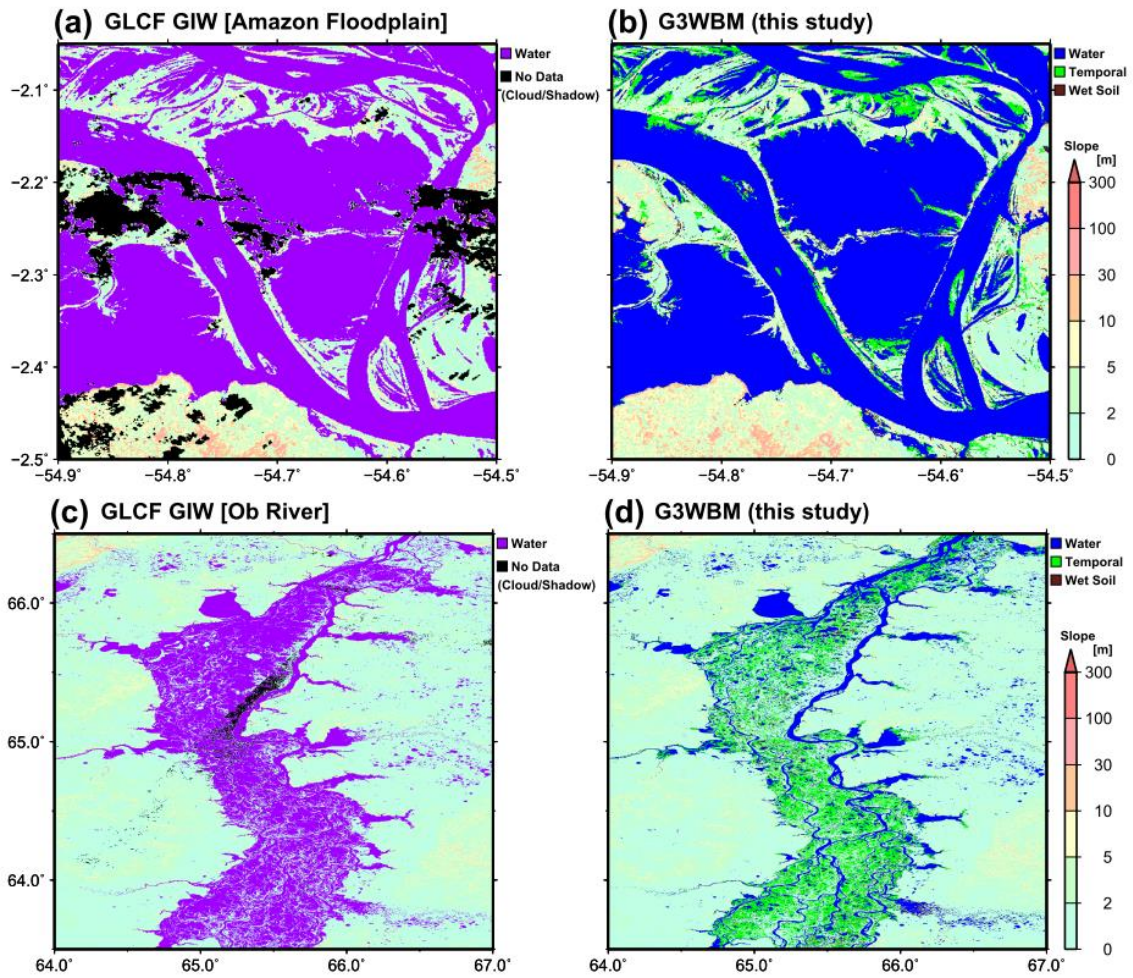


337

338 **Figure 3: Example of classification procedure, shown for the Congo River basin. (a) Band**  
 339 **5-4-2 composite images, (b) Observation confidence, (c) Water probability, (d) Water**  
 340 **frequency calculated from the four images, (e) Water mask classification. In Figure 3e,**  
 341 **blue and green represent permanent water bodies and temporal water-covered areas,**  
 342 **while background colors represent elevation gradient of land pixels.**

343 From here on, we show the results of applying the developed algorithm to all GLS images at  
344 the global scale. Results of selected regions are shown in this paper, but images of other regions  
345 can be accessed online (<http://hydro.iis.u-tokyo.ac.jp/~yamada/G3WBM/>).

346 In order to show the differences between the new and previous water body maps and the  
347 importance of using multi-temporal images, classification results in floodplains along the  
348 Amazon and Ob Rivers are shown in Figure 4. Figure 4a illustrates water bodies of the GLCF  
349 GIW in the Amazon floodplain (around W54.6, S2.3). Generally, the GLCF GIW accurately  
350 captures water bodies, but some observation gaps due to cloud covers were found. Conversely,  
351 no observation gaps were found in the new water body map (Figure 4b) because clouds were  
352 removed by overlaying multi-temporal images. Figures 4c and 4d illustrate water bodies in a  
353 downstream reach of the Ob River. Because water frequency was not considered, river channels  
354 and floodplains were lumped together in the GLCF GIW. Conversely, river channels and  
355 floodplains were represented separately in the new water body map. Given that river channels  
356 and floodplains show different bathymetry, flow dynamics and ecosystems characteristics, we  
357 believe river-floodplain separation in the new database will be useful in various research fields.



358

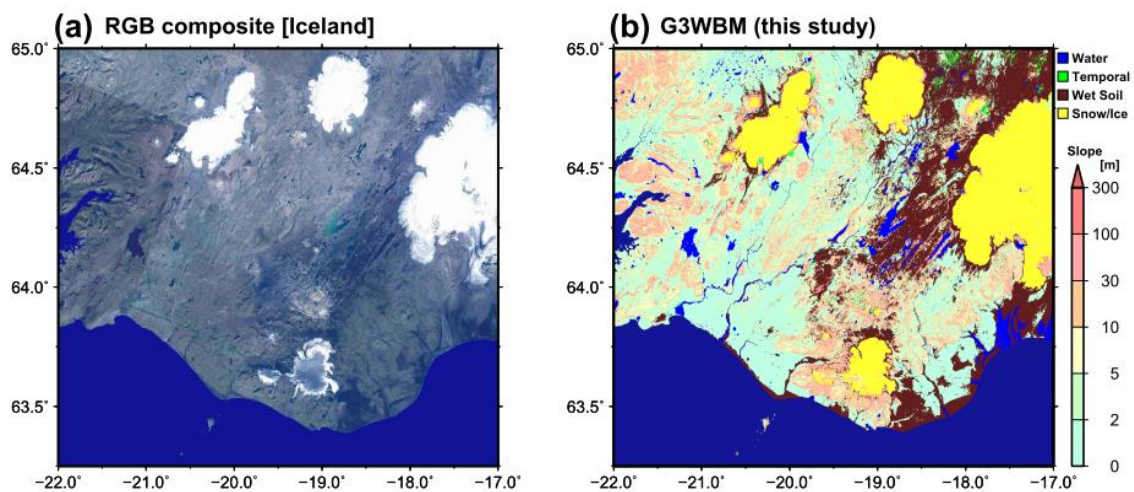
359 **Figure 4: Water bodies represented in GLCF GIW (a, c) and in G3WBM (b, d). In (a, c)**  
 360 **observation gaps due to cloud and cloud shadow are shown by black. In (b, d), permanent**  
 361 **water bodies are represented by blue, while temporal water-covered areas are shown by**  
 362 **green.**

363

Then, we validated the accuracy of the land type classification (described in Section 3.4) by  
 364 checking the results in regions where water, wet soil and snow cover are coexistent. A region of  
 365 southern Iceland was selected for this purpose. The RGB composite image and land type  
 366 classification results are shown in Figure 5. The RGB composite was created by taking the  
 367 minimum reflectance from multiple scenes in order to remove temporal cloud or ice/snow  
 368 covers. In general, the G3WBM accurately captured water bodies, including those most  
 369 commonly challenging e.g. lakes on glacier edges (e.g. W19.85, N64.60 and W17.35, N64.15),  
 370 lakes above wet lava rocks (e.g. areas around W18.8, N64.1) and lakes in the valleys between



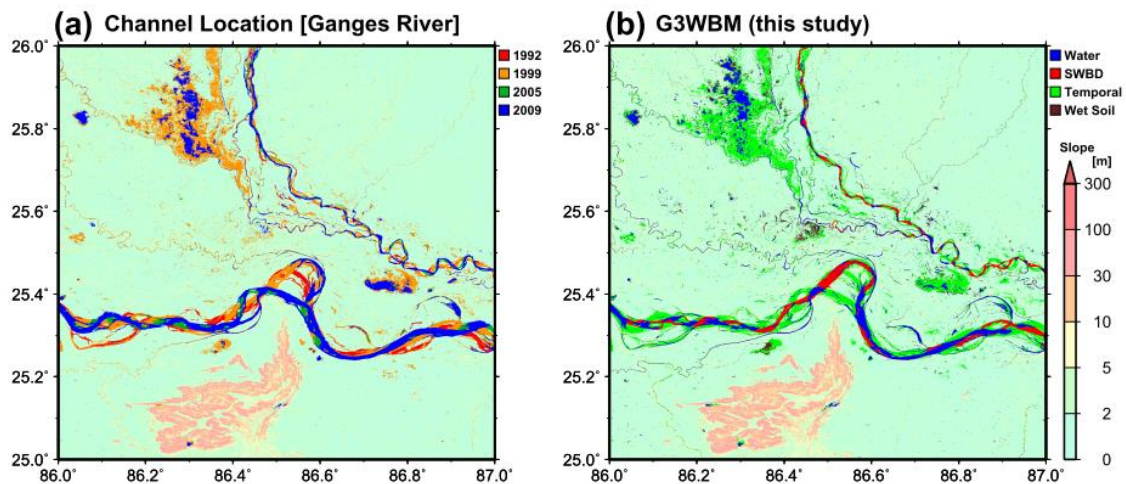
371 high mountains (e.g. W21.45, N64.5). The developed algorithm also succeeded in excluding  
 372 rocks on glaciers (e.g. W17.2 N64.2) which sometimes show similar reflectance characteristics  
 373 to water. However, boundaries between permanent water bodies and surrounding wet soils were  
 374 not clearly represented in coastal areas, probably because of a shallow groundwater table (e.g.  
 375 rivers around (W17.5, N63.8). The classification in wet coastal regions is difficult because both  
 376 water body and wet soil show a high NDWI and also because the topography is flat. It should be  
 377 noted here that the proposed method was designed for accurate delineation of permanent water  
 378 bodies, and therefore, there might be some misclassification between ice, wet soil and temporal  
 379 water-covered areas (e.g. rocks on a glacier were classified as temporal water-covered areas at  
 380 W17.35, N64.40).



381  
 382 **Figure 5: Southern Iceland region with the coexistence of water, wet soil and snow cover.**  
 383 **(a) RGB composite image, (b) and land type classification. Permanent water bodies,**  
 384 **temporal water-covered areas, wet soil, and ice/snow are represented by blue, green,**  
 385 **brown and yellow, respectively.**

386 Figure 6 illustrates a middle reach of the Ganges River, as an example of regions where  
 387 channel connectivity correction using the SWBD (Section 3.5) was required. Temporal change  
 388 of channel locations from 1992 to 2009 was calculated from eight GLS images (i.e. GLS1990,  
 389 GLS2000, GLS2005 and GLS2010 images for path 140 rows 042-043). Because the channel  
 390 location is not stable, most river segments were classified as temporal water-covered areas

391 (green pixels in Figure 6b). Disconnected channels are not ideal for hydrological research,  
 392 therefore a flow connectivity correction was performed using the SWBD water mask. Here we  
 393 can see that gaps in permanent water bodies (see discontinuous channel colored with blue in  
 394 Figure 6b) were filled by the SWBD water masks (red in Figure 6b). Please note that the SWBD  
 395 represents the water extent in February 2000, therefore, some water bodies of the SWBD might  
 396 correspond to temporal water-covered areas. This might result in a small overestimation of  
 397 permanent water bodies in the modified water body map, but we decided that the benefit of  
 398 ensuring channel continuity is greater than the disadvantage of the overestimation. Channel  
 399 connectivity correction was only performed below 60N coinciding with the SWBD coverage.  
 400 The modification was not required above 60N as almost no connectivity problems were found  
 401 in boreal regions. Of course, for geomorphological studies, the changing channel location  
 402 information observed over the GLCF epochs may be of significant value in its own right.

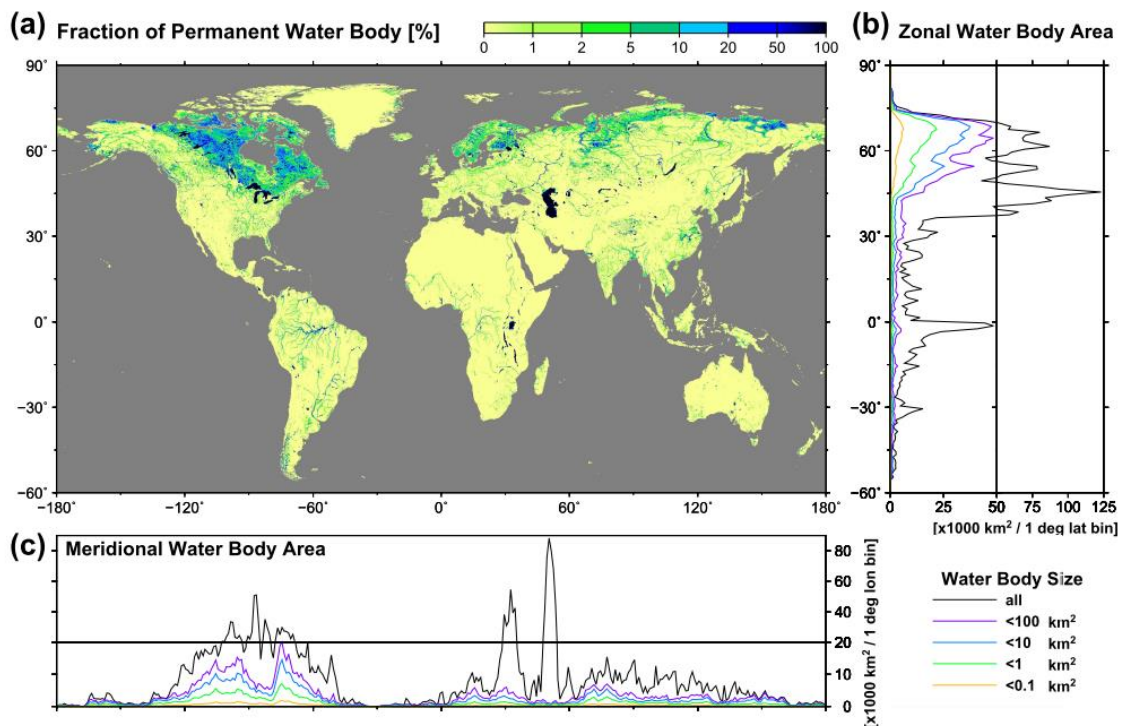


403

404 **Figure 6: (a) Channel location change in the Ganges River and (b) result of water body**  
 405 **classification. Channel locations in 1992, 1999, 2005 and 2009 are shown by red, orange,**  
 406 **dark green and blue, respectively in (a). Permanent water bodies and temporal**  
 407 **water-covered areas are shown by blue and green in (b), while overlapping SWBD water**  
 408 **mask is shown in red.**

409 A global distribution of permanent water bodies is illustrated in Figure 7. The percentage of  
 410 permanent water bodies within 0.01 degree grid boxes is shown in Figure 7a, whilst the

411 zonal/meridional total water body areas per 1 degree latitude/longitude bin are shown in Figures  
 412 6b and 6c. In total, 3.25 million km<sup>2</sup> were classified as permanent water bodies, which is about  
 413 2.4% of the total inland area (including the Caspian Sea). The aggregation of smaller water  
 414 bodies occasionally occupy more than 20% of the area of 0.01 degree grid boxes (grids colored  
 415 with blue or dark blue in Figure 7a). It can be seen that relatively small water bodies, i.e. lake  
 416 size <100 km<sup>2</sup> (purple lines in Figures 6b and 6c) are concentrated mainly in boreal regions (i.e.  
 417 Canada, Scandinavia, Finland, West and North Siberian plain, Kolyma and Indigirka River  
 418 basins). The second peak is in the Tibetan Plateau. This distribution pattern is consistent with  
 419 previous studies (e.g. Lehner and Döll, 2004; Fluet-Chouinard et al., 2015). With the exception  
 420 of boreal regions and the Tibetan Plateau, the zonal total water body area is dominated by very  
 421 large water bodies (black lines in Figures 6b and 6c), such as the North American Great Lakes,  
 422 the Caspian Sea, lakes in the African Rift Valley, and the Amazon and Congo Rivers.



423  
 424 **Figure 7: Global distribution of permanent water bodies. (a) Fraction of permanent water**  
 425 **body within 0.1 degree grid boxes. (b) Zonal and, (c) meridional total water body area per**  
 426 **1 degree latitude/longitude bin.**

## 427 **5. Discussion**

### 428 **5.1 Importance of multi-temporal analysis**

429 The global distribution of temporal water-covered areas is illustrated in Figure 8. Temporal  
430 water-covered areas are concentrated in large river floodplains (e.g. the Ob, Lena, Amazon and  
431 Ganges Rivers), boreal climate regions (e.g. northern Canada and northern Siberia) and arid  
432 regions (e.g. inland Australia and Central Asia). Temporal water-cover in boreal regions is  
433 likely to be dominated by snow melt because the acquisition timing of the GLS images in the  
434 boreal region were June to August (Gutman et al, 2013), which overlaps with the snow melt  
435 season in high latitude zones (Armstrong et al., 2005). The area around the Aral Sea is classified  
436 as a temporal water-covered area because it had been covered by open water in earlier GLS  
437 images but was dried up in later images. The global summation of temporal water-covered areas  
438 was 0.49 million km<sup>2</sup>, about 15% of the global permanent water body area (see Table 3). These  
439 areas could be misclassified as permanent water bodies if only flooded images were used in the  
440 water body mask development.

441 Global total area for each land classification type was calculated for the G3WBM and the  
442 GLCF GIW (Feng et al., 2015) and summarized in Table 3. Among the 3.81 million km<sup>2</sup> of  
443 inland water area in the GLCF GIW, 2.92 million km<sup>2</sup> is classified as permanent water in the  
444 G3WBM but other areas are classified as temporal water-covered area (0.17 million km<sup>2</sup>) or as  
445 non-water surface (0.71 million km<sup>2</sup>). The classification discrepancy between water and land  
446 (i.e. water in one database but land in the other) is probably due to the difference in spatial  
447 resolutions. However, the 0.17 million km<sup>2</sup> areas treated as water in the GLCF GIW but  
448 temporal water-covered area in the G3WBM was detected because multi-temporal scenes were  
449 used in the G3WBM. This indicates the importance of the water frequency analysis in creating  
450 global water body maps. Furthermore, the GLCF GIW includes the 3.61 million km<sup>2</sup> of no-data  
451 areas which are mainly due to cloud or cloud shadow. Though most of the no-data areas are  
452 considered to be land, the GLCF GIW missed some true water bodies (as shown in Figure 4a).

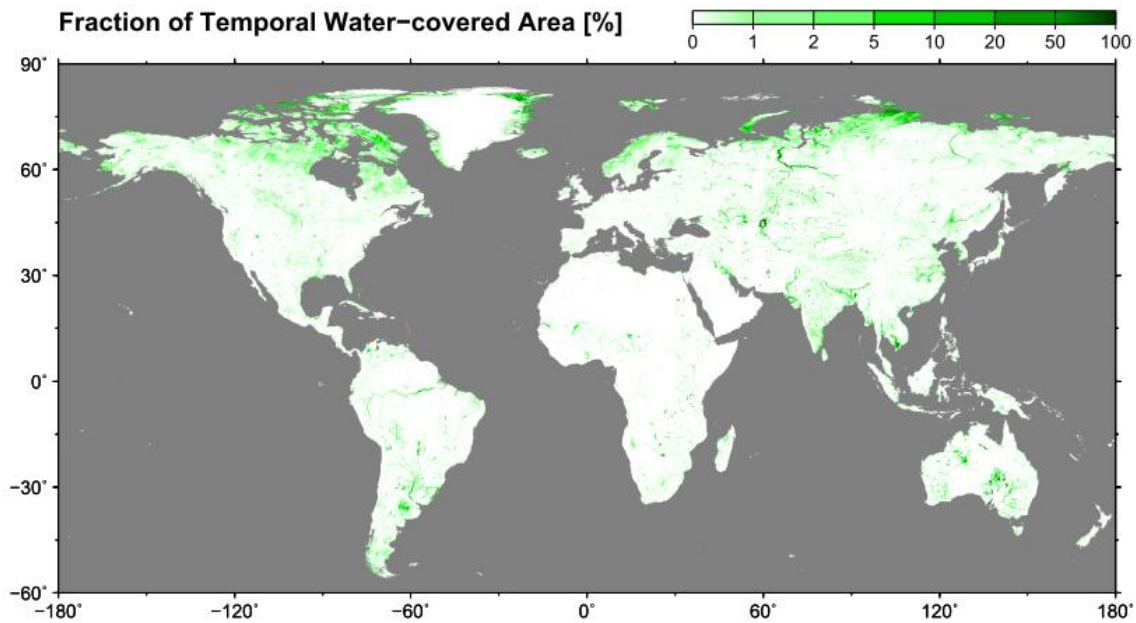


453 This also illustrates the importance of using multi-temporal images for eliminating gaps in water  
 454 body mask.

455 Please note that the water frequency analysis in this study was mainly performed to delineate  
 456 an accurate permanent water body mask by excluding temporal water-covered areas. The  
 457 developed method did not intend to accurately delineate all temporal water-covered areas on the  
 458 earth. Whether temporal water-covered areas could be detected or not, is decided by images  
 459 used in the analysis. If flood images are not included in the GLS database, it is, of course, not  
 460 represented as a temporal water-covered area in the developed database.

461 **Table 3. Confusion matrix of global inland area classification between G3WBM and GLCF**  
 462 **GIW.**

Global total area [x1000 km <sup>2</sup> ]		GLCF GIW			Total
		Water	Land	No Data	
G3WBM (this study)	Permanent Water Body	2,924	245	72	<b>3,240</b>
	Temporal Flood Area	176	303	14	<b>493</b>
	Other Land Types	709	126,998	3,520	<b>131,228</b>
<b>Total</b>		<b>3,809</b>	<b>127,545</b>	<b>3,606</b>	



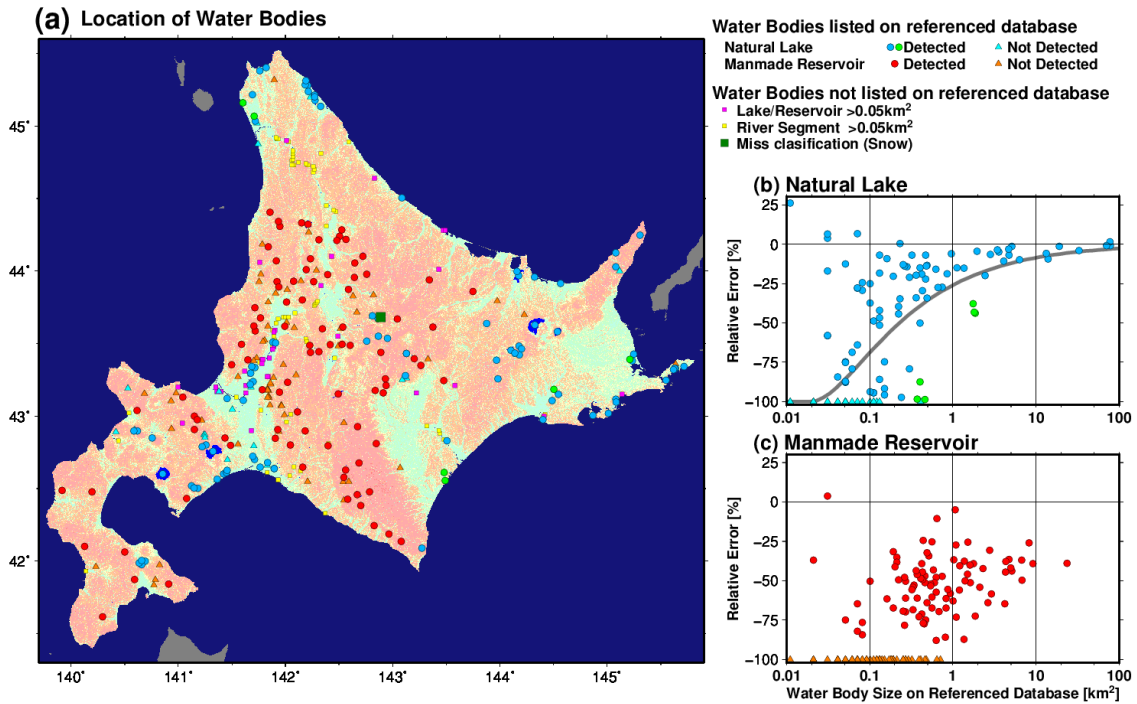
463

464 **Figure 8: Global distribution of temporal water-covered areas. Percentage of temporal**  
 465 **water-covered areas in each 0.1 degree grid box is shown.**

## 466 **5.2 Accuracy of water body detection**

467 We performed extensive validation on Hokkaido Island, northern Japan (Figure 9a) to  
 468 estimate the accuracy of the water body detection. The delineated water body area in the  
 469 validation domain was 472 km<sup>2</sup>, about 0.6% of the area of Hokkaido Island (77,984 km<sup>2</sup>). The  
 470 accuracy of excluding non-water land types from actual water body area was first examined. We  
 471 checked whether each water body in G3WBM corresponded to actual rivers/lakes or not, by  
 472 plotting all permanent water bodies larger than 0.05 km<sup>2</sup> onto topographical maps and  
 473 space/airborne photos using Google Maps. There were 280 water bodies larger than 0.05 km<sup>2</sup> in  
 474 the G3WBM (circle and square plots in Figure 9). We found only one exception which did not  
 475 correspond to an actual water surface (the dark green square in Figure 9a). The commission  
 476 error was located at the caldera of Taisetsu-zan Mountain (E142.88, N43.68), where snow cover  
 477 and wet lava soil exist together. All water bodies, except for this commission error,  
 478 corresponded to rivers and lakes on the topographic map or space/airborne photos. This result  
 479 suggested that the proposed method can accurately distinguish water-like land type (e.g. snow,

480 wet soil, shadow) from actual water bodies. Therefore, the overestimation of water bodies in the  
 481 G3WBM was anticipated to be very small.



482

483 **Figure 9: (a) Location of water bodies on Hokkaido Island, Japan. (b) and (c) Relative**  
 484 **error of detected natural/manmade water bodies to lake/reservoir database. Grey lines in**  
 485 **(b) represent an expected error due to coastline misclassification for circle-shape lakes.**

486 We then compared the surface area of individual natural lakes found using our newly  
 487 developed map against an existing database. We used the GIS database of natural lakes  
 488 developed by Hokkaido Research Organization (available at <http://envgis.ies.hro.or.jp/>). All  
 489 lakes registered in the GIS database (117 lakes excluding lagoons which were treated as ocean  
 490 in the G3WBM) were used in the comparison. The size of referenced lakes varied from 77.76  
 491 km<sup>2</sup> to 0.01 km<sup>2</sup>. Among the 117 referenced lakes, 94 lakes were detected in the G3WBM (blue  
 492 and green circles in Figure 9) but 23 lakes were missed (light blue triangles in Figure 9). The  
 493 relative error of each lake area is plotted on Figure 9b. It was found that surface areas were  
 494 underestimated in most lakes, except for very small ones which consisted of two or three pixels.  
 495 Lakes with relatively large errors (green circles in Figure 9) were found to be shallow marsh

496 with a large surface area variation (Penketo Marsh; E141.71, N45.07, Shirarutoro Marsh;  
497 E144.50, N43.18, and Oikamanai Lake; E143.45, N42.56) and lakes covered by dense aquatic  
498 vegetation (Kimonto Marsh; E143.48, N42.61, Kanekinto Marsh; E145.21, N43.39, and Junsai  
499 Marsh; E141.60, N45.16). The discrepancy in shallow marsh with large surface area variation  
500 can be explained by the timing of observations. Underestimation in vegetated lakes was caused  
501 by the mixing of water and vegetation. As pixels covered by aquatic vegetation (such as water  
502 lily) have lower NDWI and higher NDVI than open water, most of them were judged to be wet  
503 soil/vegetation. Underestimation in other lakes can be mainly explained by the treatment of  
504 shoreline pixels. Given that water and land are mixed in shoreline pixels, they tend to be judged  
505 as wet soil because of their moderate NDWI. The ratio of shoreline pixels to all lake pixels  
506 becomes larger for smaller lakes, thus a larger underestimation was observed in smaller lakes in  
507 Figure 9b. The underestimation expected from shoreline misclassification was calculated by  
508 assuming all coastline pixels of a circle-shaped lake had been judged to be non-water. The  
509 expected error (the gray line in Figure 9b) well explain the actual underestimation ratio for each  
510 size class. Similar to small lakes, rivers narrower than one pixel size (about 90 m at the equator)  
511 were not well represented in the G3WBM.

512 We also compared the lake surface area of manmade reservoirs from the G3WBM against an  
513 existing dam database. All manmade reservoirs constructed before 2000 as listed in the  
514 handbook of Japanese dams (Japan Dam Association, 2014) were used in the comparison. In the  
515 delineated water body map, 93 out of 152 reservoirs were represented in the G3WBM (red  
516 circles in Figure 9) but 59 reservoirs were missing (orange triangles in Figure 9). The relative  
517 error of lake surface area is plotted on Figure 9c. Similar to natural lakes, smaller reservoirs  
518 generally showed a larger underestimation of area. However, the underestimation ratio was  
519 larger in manmade reservoirs than natural lakes. This is probably because reported lake areas in  
520 the dam handbook denote surface areas at maximum storage capacity. Actual dam storage is  
521 usually smaller than the maximum capacity, therefore the reservoir surface areas are likely to be

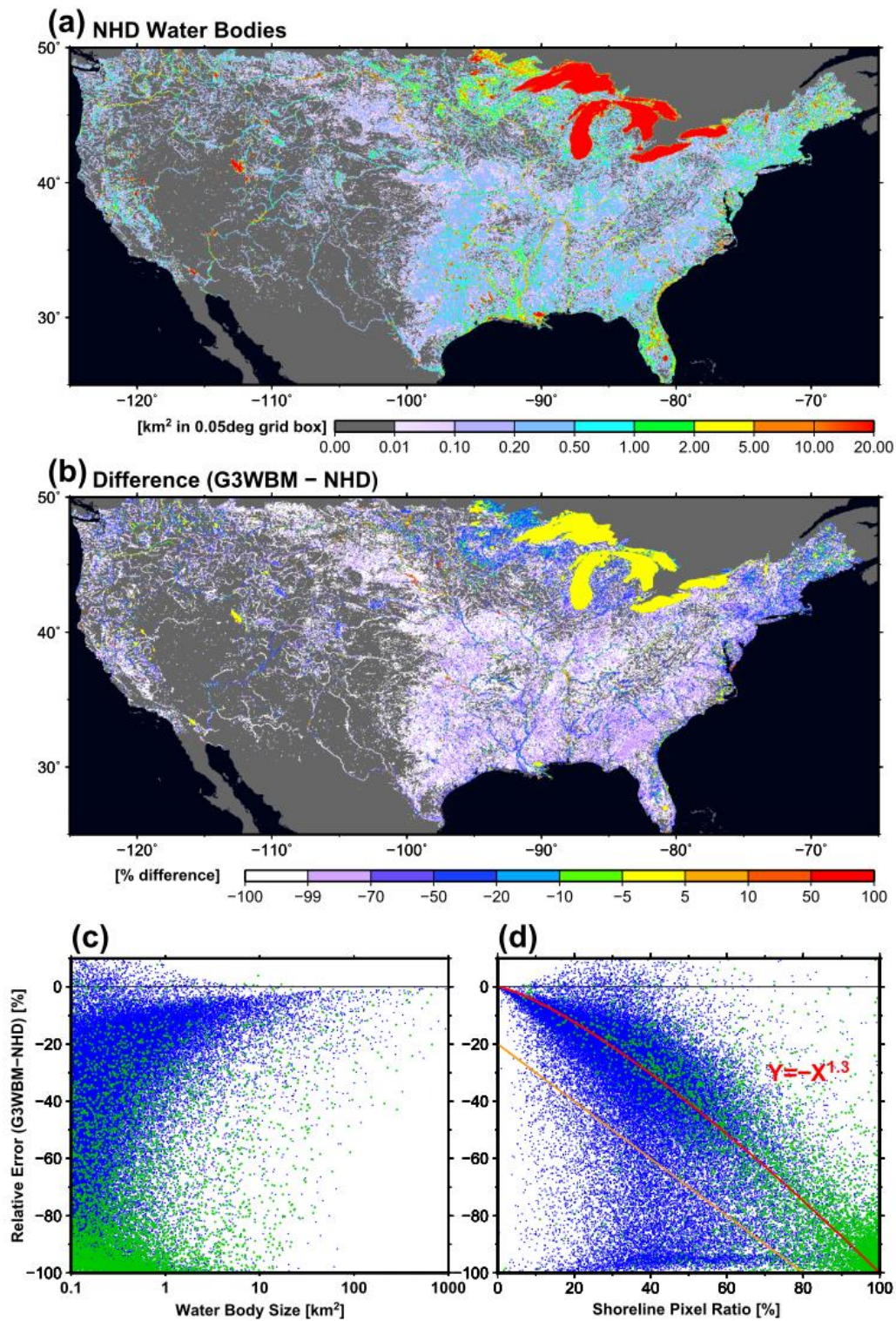
522 underestimated using observations, and this makes classification accuracy of manmade reservoir  
523 areas in Hokkaido particularly challenging. Another reason for underestimation may be due to  
524 the locations of manmade reservoirs. While natural lakes tend to be located in flat regions,  
525 manmade reservoirs are generally created in mountainous areas. As we used elevation gradient  
526 of the DEM for separating shadow from water bodies, some reservoirs were mistakenly  
527 classified as shadows. In order to improve the classification accuracy, higher resolution  
528 topographic data is needed, especially in mountainous area.

529 The accuracy of water body delineation was also validated using high quality geospatial data  
530 of the contiguous United States. The U.S. Geological Survey National Hydrography Dataset  
531 (NHD) (Simley and Carswell, Jr., 2009) (Figure 10a) was selected for this purpose. Given that  
532 the NHD is high-resolution vector data of water bodies based on the U.S. topography maps, its  
533 accuracy is considered to be adequate for validation of satellite-derived water maps. The NHD  
534 “waterbody” and “river stream area” polygons were converted to a 1 arc-second raster, and then  
535 water body areas were compared between the NHD and the G3WBM (Figure 10b). The NHD  
536 polygons were converted to a higher resolution raster (1 arc-sec) than the G3WBM because they  
537 were treated as “truth” data for validation purpose. It was found that large water bodies (red in  
538 Figure 10a) were well represented in the G3WBM (yellow color in Figure 10b), while most  
539 small water bodies ( $<0.1 \text{ km}^2$ , pale violet colors in Figure 10a) were not captured (white in  
540 Figure 10b). Overestimation of water body area was limited to some flood prone regions (red  
541 colored area in Figure 10b), so that commission error is expected to be very small in the  
542 G3WBM.

543 Figure 10c shows the relative water area error of 80,312 water bodies in the NHD whose size  
544 is larger than  $0.1 \text{ km}^2$ . Blue dots represent “waterbody” features in the NHD database (i.e. lakes,  
545 ponds, and reservoirs), while green dots represent “river stream area”. It was found that about  
546 70% of water bodies  $>1 \text{ km}^2$  show relative water area error smaller than 25%. Similar to the  
547 case of Hokkaido Island (Figure 9b), underestimation error was larger for smaller water bodies.

548 In general, lakes, ponds, and reservoirs are better delineated compared to river stream areas. In  
549 order to analyze why water body area was underestimate, the ratio of shoreline pixels to water  
550 body pixels within each water body was calculated and plotted against the relative water area  
551 error (Figure 10d). A strong relationship was observed between the shoreline pixel ratio and the  
552 relative water area error (the red line in Figure 10d). This suggests that the underestimation of  
553 water body area is mainly due to the difficulty of classifying shoreline pixels on water-land  
554 boundaries. Thus, narrow river segments or lakes in mountainous valley regions are not well  
555 represented in the G3WBM because they have relatively long shorelines compared to their  
556 water body size. We visually checked the location of 1,466 water bodies  $>1 \text{ km}^2$  whose relative  
557 error is more than 20% larger than the shoreline pixel ratio (i.e. below the orange line in Figure  
558 10d). It was found that these large errors mainly correspond to water bodies with large surface  
559 area fluctuation (e.g. floodplains, salt marshes, and reservoirs with frequent water level change).  
560 Given that the proposed algorithm was designed to detect only permanent water bodies, this  
561 underestimation was expected because temporal change of water body area was not included in  
562 the NHD. However, we also found that some omission errors were caused by vegetation  
563 coverage over permanent water bodies (e.g. swamps, algae blooms). In order to further improve  
564 water body detection accuracy, classification of vegetated water bodies should be considered, in  
565 addition to a better shoreline classification.





566

567 Figure 10: Distribution of water bodies in the NHD (a) and the difference between the  
 568 G3WBM and the NHD (b). For visualization purpose, the resolution of water body map  
 569 was converted to 0.05 degree. Scatter plots of relative water area error versus water body  
 570 size (c) and versus shoreline pixel ratio (d). Blue and green dots represent “waterbody”  
 571 and “stream area” features in the NHD database.

### 572 **5.3 Comparison of Global Water Body Area**

573 The total inland water body area (both river and lakes) in the constructed water mask  
574 database was 3.25 million km<sup>2</sup> (including the Caspian Sea at 0.36 million km<sup>2</sup>). The total water  
575 surface area of large water bodies (>100 km<sup>2</sup>) accounts for 63% of the total inland water body  
576 area, and the remaining water surface is accounted for by smaller water bodies. Lakes smaller  
577 than 0.1 km<sup>2</sup>, 1 km<sup>2</sup> and 10.0 km<sup>2</sup> account for 4%, 13 % and 26% of the total inland water body  
578 area, respectively. Given that most of the small lakes (<0.1 km<sup>2</sup>) are not well represented in the  
579 constructed database, the global total water extent is expected to be underestimated. Note that  
580 the size of a pixel is 0.0085 km<sup>2</sup> at the Equator and 0.0043 km<sup>2</sup> at 60 degree north/south.

581 Global total water body areas are compared between the 6 water body datasets in Table 4. In  
582 the case of the products based on optical sensors (i.e. MODIS and Landsat), the global water  
583 body area generally increases with the resolution of the product because smaller water bodies  
584 are detected at higher resolution. However, the global total water body area is also affected by  
585 the coastline definition and treatment of temporal water-covered areas (e.g. floodplains, salt  
586 marsh). For example, the G3WBM shows a relatively smaller area compared to other products  
587 because floodplains and salt marsh are excluded from permanent water bodies. The global water  
588 body area of the GLOWABO (5.37 million km<sup>2</sup>) (Verpoeter et al., 2014) is significantly larger  
589 than other products based on Landsat or MODIS (between 3.25 and 3.65 million km<sup>2</sup>). This is  
590 probably because small water bodies are represented at the 0.5 arc-second resolution, but  
591 without direct comparison of the products, the exact reason for this large difference is unclear.  
592 The global water body area of the GIEMS-D15 (Fluet-Chouinard et al. 2015) is the largest  
593 among the all databases, probably due to the downscaling procedure. The GIEMS-D15 was  
594 generated by downscaling 25-km resolution water extent data (Papa et al., 2010) onto a 15  
595 arc-second topography, which may cause over-representation of rivers and lakes smaller than  
596 the 15 arc-second pixel size (about 500 m at the equator). The statistical estimate by Downing et  
597 al. (2006) was analyzed to be an overestimation (McDonald et al., 2012), so that the global



598 water estimations by the three databases (GLCF MODIS, GLCF GIW, and G3WBM) are  
 599 considered to be consistent.

600 **Table 4. Comparison of global total water body area between 5 databases.**

Water body database	Source	Resolution	Global water area	Cutoff Threshold
GLCF MODIS <sup>a</sup>	MODIS	7.5 sec	3.29 million km <sup>2</sup>	N/A
G3WBM (permanent water)	Landsat	3 sec	3.25 million km <sup>2</sup>	1 pixel (~0.008 km <sup>2</sup> )
GLCF GIW	Landsat	30 m	3.65 million km <sup>2</sup>	5 pixels (~0.005 km <sup>2</sup> )
GLOWABO <sup>b</sup>	Landsat	0.5 sec	5.37 million km <sup>2</sup>	0.002 km <sup>2</sup>
GIEMS-D15 (annual min)	Multi-satellite	15 sec	6.5 million km <sup>2</sup>	N/A
Downing et al. 2006 <sup>c</sup>	Statistical	-	4.2 million km <sup>2</sup>	0.001 km <sup>2</sup>

601 <sup>a</sup>The water body area of GLCF MODIS was calculated by the authors because it's not available  
 602 in the description paper (Carroll et al., 2009).

603 <sup>b</sup>The water body area of the Caspian Sea was added to the GLOWABO for comparison.

604 <sup>c</sup>Downing et al. excluded river water surface from global water body area.

## 605 **5.4 Possibility of further improvement**

606 We restricted the resolution of G3WBM to 3 arc-second due to limitations in human and  
 607 computational resources. However, given that the original resolution of Landsat images is about  
 608 1 arc-second, developing a global 1 arc-second water body map with water frequency  
 609 information is certainly possible. Given that the underestimation of lake area in G3WBM is  
 610 likely due to omission of shoreline water pixels, the accuracy of water classification is  
 611 anticipated to increase in a higher-resolution water body map.

612 Even with the large number of scenes used, not all seasonal or extreme flood events will be  
 613 captured in the water map developed here. Part of the reason for this will be due to the fact that  
 614 cloud free scenes from leaf-on growing seasons were selected in the GLS collection, meaning  
 615 that all the GLS images utilized come from the same season and therefore may “miss” flooding  
 616 in other seasons. Given that temporary water bodies are hotspots for biodiversity and  
 617 biogeochemical processes, accurate estimate of global temporal water extent is essential in this  
 618 regard. Including future images as they become available, as well as broadening the number of

619 images processed to include non-GLCF scenes may help reduce these issues, but will bring a  
620 higher computation cost and may increase observational uncertainty. Furthermore, while most  
621 temporal water-covered areas represent seasonal flooding, some represent long-term trends  
622 (such as shrinking of the Aral Sea, construction of dams, disappearing water bodies in Alaska  
623 and Siberia). Separation of seasonal and long-term water body change may be important for  
624 estimating global dynamics of surface waters. In addition, it's better to use topography data  
625 consistent with the time of Landsat image acquisition, because the elevation gradient from the  
626 DEM is used for water body classification.

627 The classification algorithm could be further improved to capture water bodies more  
628 accurately. We used the classification criteria with globally-constant thresholds (as in Table 3),  
629 but the threshold could be different in different regions. For example, sediment-rich and/or  
630 turbid water tends to show lower NDWI and higher NDVI than sediment-free water, so that  
631 some sediment-rich rivers are misclassified as wet soil in G3WBM (e.g. small tributaries of the  
632 Indus River). Vegetated water surface (e.g. lakes with algal blooms, floating plants) has similar  
633 characteristics to sediment-rich water, thus it is difficult to be detected by classification criteria.  
634 Using variable thresholds (e.g. Feng et al., 2015) based on local reference water body data may  
635 be a good solution for improving classification accuracy. Shoreline pixels with land and water  
636 mixing are likely to be omitted as wet soil because they have a lower NDWI than pure water  
637 pixels. Applying an additional classification step for shoreline pixels, after determining water  
638 body pixels, may improve the overall accuracy of water body mapping because mixed shoreline  
639 pixels are considered to be a major source of water area underestimation.

640 We did not applied atmospheric correction in this study in order to reduce computational  
641 requirements. The previous study by Verpoeter et al. (2014) argued that atmospheric correction  
642 is not necessary for global water body mapping. Given that the GLCF GLS database consists of  
643 mostly-cloudless Landsat images from leaf-on growing seasons, atmospheric conditions are  
644 expected to be similar between different images and this probably decreases the need in

645 atmospheric correction. However it should be better to remove the inconsistency due to  
646 atmospheric conditions, especially when multi-temporal images are used (Song et al., .2001).  
647 Application of atmospheric correction is therefore a possible strategy for improving the  
648 accuracy of water body detection in the G3WBM.

## 649 **6. Conclusion**

650 We developed the Global 3 arc-second Water Body Map (G3WBM) using 33,890  
651 multi-temporal Landsat GLS images. In addition to the conventional land/water classification  
652 used in a previous global water body database, we separated permanent water bodies from  
653 temporal water-covered areas by calculating the frequency of water body existence from  
654 multi-temporal images. The G3WBM identified 3.25 million km<sup>2</sup> of permanent water bodies in  
655 the global inland areas, while the global total of temporal water-covered areas was 0.5 million  
656 km<sup>2</sup> (~15% of the global permanent water body area). The abundance of temporal  
657 water-covered areas suggests the importance of water frequency analysis using multi-temporal  
658 images. From the Comparison to a 30-m resolution water body map (the GLCF GIW), we  
659 concluded that the use of multi-temporal images is as important as analysis at a higher  
660 resolution for depicting global-scale dynamics of surface water bodies.

661 The accuracy of water body delineation was validated using space/airborne photos and the  
662 existing database of waterbodies in Hokkaido (Japan) and in the contiguous United States.  
663 There was almost no commission error of water bodies in the G3WBM, which suggests that the  
664 proposed classification algorithm has a very high accuracy. The areas of small lakes in the  
665 G3WBM tend to be underestimated, mainly due to the mixing of land and water in shoreline  
666 pixels, however the accuracy will be improved if a water body map is generated at higher  
667 resolution. Given that the proposed method is automated, it is not impossible to generate a  
668 global water body map at 1 arc-second (~30 m) or higher resolutions.

669       The G3WBM is distributed free of charge for research and educational purposes. Please visit  
670 the product webpage (<http://hydro.iis.u-tokyo.ac.jp/~yamadai/G3WBM>) to get access to the  
671 database.

672

## 673 **Acknowledgements**

674 This research is funded by “JSPS Grant-in-Aid for Scientific Research #26889077”. A part  
675 of the computational resources is also supported by “JSPS Grant-in-Aid for Scientific Research  
676 #23226012”. Mark Trigg’s contributions were completed under funding provided by the Willis  
677 Research Network.

## 678 **References**

- 679 Allen, G.H. & Pavelsky T.M. (2015). Patterns of river width and surface area revealed by the  
680 satellite-derived North American River Width data set, *Geophysical Research Letters.*, 42,  
681 395–402, doi:10.1002/2014GL062764.
- 682 Armstrong, R., Brodzik M., Knowles K., & Savoie M. (2005). Global Monthly EASE-Grid Snow  
683 Water Equivalent Climatology. Boulder, Colorado USA: NASA National Snow and Ice Data  
684 Center Distributed Active Archive Center.
- 685 Bridgham, S.D., Cadillo-Quiroz H., Keller J.K., & Zhuang Q., (2013). Methane emissions from  
686 wetlands: Biogeochemical, microbial, and modeling perspectives from local to global scales.  
687 *Global Change Biology*, 19(5), 1325–1346.
- 688 Carroll, M.L., Townshend J.R., Di Miceli C.M., Noojipady P., & Sohlberg R.A. (2009), A new  
689 global raster water mask at 250 m resolution, *International Journal of Digital Earth*, 2(4),  
690 291-308, doi:10.1080/17538940902951401.
- 691 Chander, G. & Markham B.L. (2003). Revised Landsat-5 TM radiometric calibration procedures, and  
692 post-calibration dynamic ranges. *IEEE Transactions on Geoscience and Remote Sensing*, 41,  
693 2674–2677, doi: 10.1109/TGRS.2003.818464
- 694 Chander, G, Markham B.L., & Helder D.L. (2009). Summary of current radiometric calibration  
695 coefficients for Landsat MSS, TM, ETM+, and EO-1 ALI sensors. *Remote Sensing of*  
696 *Environment*, 113, 893–903, doi:10.1016/j.rse.2009.08.011.
- 697 Cole, J. J., Prairie Y.T., Caraco N.F., McDowell W.H., Tranvik L.J., Striegl R.G., Duarte C.M.,  
698 Kortelainen P., Downing J.A., Middelburg J.J., & Melack J. (2007). Plumbing the Global  
699 Carbon Cycle: Integrating Inland Waters into the Terrestrial Carbon Budget, *Ecosystems*, 10 (1),  
700 172–184, doi: 10.1007/s10021-006-9013-8.
- 701 Downing, J.A., Prairie Y.T., Cole J.J., Duarte C.M., Tranvik L.J., Striegl R.G., McDowell W.H.,  
702 Kortelainen P., Caraco N.F., Melack J.M., & Middelburg J.J. (2006). The Global Abundance  
703 and Size Distribution of Lakes, Ponds, and Impoundments, *Limnology and Oceanography*, 51  
704 (5), 2388-2397.

- 705 Downing, J. A. (2010). Emerging global role of small lakes and ponds: little things mean a lot,  
706 *Limnetica*, 29 (1), 9-24.
- 707 Downing, J.A., Cole J.J., Duarte C.A., Middelburg J.J., Melack J.M., Prairie Y.T., Kortelainen P.,  
708 Striegl R.G., McDowell W.H., & Tranvik L.J. (2012). Global abundance and size distribution of  
709 streams and rivers, *Inland Waters*, 2 (4), 229-236
- 710 Farr, T. G., et al. (2007). The Shuttle Radar Topography Mission. *Review of Geophysics*. 45, RG2004,  
711 doi:10.1029/2005RG000183.
- 712 Feng, M., Sexton J.O., Channan S., & Townshend J.R. (2015). A global, high-resolution (30 m)  
713 inland water body dataset for 2000: first results of a topographic-spectral classification  
714 algorithm, *International Journal of Digital Earth*, published online,  
715 DOI:10.1080/17538947.2015.1026420
- 716 Fluet-Chouinard, E., Lehner B., Rebelo L.M., Papa F., & Hamilton S.K. (2015). Development of a  
717 global inundation map at high spatial resolution from topographic downscaling of coarse-scale  
718 remote sensing data, *Remote Sensing of Environment*, 158, 348-361,  
719 doi:10.1016/j.rse.2014.10.015
- 720 Gutman, G., Huang C., Chander G., Noojipady P., & Masek J.G. (2013). Assessment of the  
721 NASA-USGS Global Land Survey (GLS) datasets, *Remote Sensing of Environment*, 134,  
722 249–265, doi: 10.1016/j.rse.2013.02.026.
- 723 Irish, R. (2000). Landsat 7 automatic cloud cover assessment: Algorithms for multispectral,  
724 hyperspectral, and ultraspectral imagery, *Proceedings of SPIE*, 4049, 348–355.
- 725 Japan Dam Association (2014). Dam Nenkan 2014 (in Japanese), Tokyo.
- 726 Ji, L., Zhang L., & Wylie B. (2009). Analysis of dynamic thresholds for the normalized difference  
727 water index, *Photogrammetric Engineering and Remote Sensing*, 75 (2009), 1307–1317.
- 728 Lehner, B. & Döll P. (2004). Development and validation of a global database of lakes, reservoirs  
729 and wetlands, *Journal of Hydrology*, 296(1–4), 1–22.
- 730 Maxwell, S.K., Schmidt G.L., & Storey J.C. (2007). A multi-scale segmentation approach to filling  
731 gaps in Landsat ETM+ SLC-off images, *International Journal of Remote Sensing*, 28(23),  
732 5339–5356. doi:10.1080/014311601034902.
- 733 McDonald, C.P., Rover J.A., Stets E.G., & Striegl R.G. (2012). The regional abundance and size  
734 distribution of lakes and reservoirs in the United States and implications for estimates of global  
735 lake extent, *Limnology and Oceanography*, 57 (2),597-606, doi: 10.4319/lo.2012.57.2.0597.
- 736 McFeeters, S.K. (1996). The use of Normalized Difference Water Index (NDWI) in the delineation  
737 of open water features, *International Journal of Remote Sensing*, 17(7),1425–1432.
- 738 NASA/NGA (2003). SRTM Water Body Data Product Specific Guidance, Version 2.0, available  
739 online: [http://dds.cr.usgs.gov/srtm/version2\\_1/SWBD/SWBD\\_Documentation/](http://dds.cr.usgs.gov/srtm/version2_1/SWBD/SWBD_Documentation/)
- 740 Oki, T. & Kanae S. (2006). Global hydrological cycles and world water resources, *Science*, 313,  
741 1068 – 1072, doi:10.1126/science.1128845.

- 742 O'Loughlin, F., Trigg M.A., Schumann G.J.-P., & Bates P.D. (2013). Hydraulic characterization of  
743 the middle reach of the Congo River, *Water Resources Research*, 49, 5059–5070,  
744 doi:10.1002/wrcr.20398.
- 745 Palmer, S.C.J., Kutser T., & Hunter P.D. (2015). Remote sensing of inland waters: Challenges,  
746 progress and future directions, *Remote Sensing of Environment*, 157, 1-8, doi:  
747 10.1016/j.rse.2014.09.021.
- 748 Papa, F., Prigent C., Aires F., Jimenez C., Rossow W.B., & Matthews E. (2010). Interannual  
749 variability of surface water extent at the global scale, 1993 – 2004, *Journal of Geophysical*  
750 *Research*, 115, D12111, doi:10.1029/2009JD012674.
- 751 Pappenberger, F., Dutra E., Wetterhall F., & Cloke H.L. (2012). Deriving global flood hazard maps  
752 of fluvial floods through a physical model cascade, *Hydrology and Earth System Science*, 16,  
753 4143-4156, doi:10.5194/hess-16-4143-2012.
- 754 Prigent, C., Papa F., Aires F., Rossow W.B., & Matthews E. (2007). Global inundation dynamics  
755 inferred from multiple satellite observations, 1993–2000, *Journal of Geophysical Research*, 112,  
756 D12107, doi:10.1029/2006JD007847.
- 757 Sampson, C.C, Smith A.M., Bates P.D., Neal J.C., Alfieri L., & Freer J.E. (2015). A high-resolution  
758 global flood hazard model, *Water Resources Research*, published online,  
759 doi:10.1002/2015WR016954
- 760 Sjögersten, S., Black C.R., Evers S., Hoyos-Santillan J., Wright E.L., & Turner B.L. (2014). Tropical  
761 wetlands: A missing link in the global carbon cycle?, *Global Biogeochemical Cycles*, 28,  
762 1371–1386, doi:10.1002/2014GB004844.
- 763 Song, C., Woodcock C.E., Seto K.C., Lenney M.P., & Macomber S.A. (2001). Classification and  
764 change detection using Landsat TM data: When and how to correct atmospheric effects?  
765 *Remote Sensing of Environment*, 75, 230-244, doi:10.1016/S0034-4257(00)00169-3.
- 766 Verpoeter, C., Kutser T., Seekell D.A., & Tranvik L.J. (2014). A global inventory of lakes based on  
767 high-resolution satellite imagery, *Geophysical Research Letters*, 41, 6396 – 6402,  
768 doi:10.1002/2014GL060641.
- 769 Warmerdam, F. (2008). The Geospatial Data Abstraction Library, *Open Source Approaches in*  
770 *Spatial Data Handling*, Springer, 87-104.
- 771 Xu H (2006). Modification of normalised difference water index (NDWI) to enhance open water  
772 features in remotely sensed imagery, *International Journal of Remote Sensing*, 27 (14),  
773 3025-3033, doi:10.1080/01431160600589179.
- 774 Yamazaki, D., O ' Loughlin F., Trigg M.A., Miller Z.F., Pavelsky T.M., & Bates P.D. (2014a).  
775 Development of the global width database for large rivers, *Water Resources Research*, 50,  
776 doi:10.1002/2013WR014664.
- 777 Yamazaki, D., Sato T., Kanae S., Hirabayashi Y., & Bates P.D. (2014b). Regional flood dynamics in  
778 a bifurcating mega delta simulated in a global river model, *Geophysical Research Letters*, 41,  
779 doi:10.1002/2014GL059744.

## 780 **Appendix**

### 781 **A.1 SLC gap filling**

782 Landsat7 images after 31<sup>st</sup> May 2003 have striped gaps due to the failure of the Scan Line  
783 Corrector (SLC). This could result in striping patterns in water body classification, thus we  
784 removed the SLC gaps by the following interpolation method. After calculating water frequency,  
785  $F_w$ , using multiple Landsat images (Section 3.2), pixels with  $F_w > 0.1$  were marked as  
786 potential water bodies. Remaining pixels were marked as potential land areas. Then, SLC gap  
787 filling was applied for each Landsat scene, using this extra information from non-SLC-gap  
788 scenes. If a pixel within an SLC gap was a potential water body in non-SLC-gap scenes,  
789 reflectance values were copied from its nearest water body pixel (outside the gap), and for  
790 potential land areas the nearest potential land pixel reflectance was copied. This interpolation is  
791 based on the assumption that reflectance values must be similar within adjacent water body  
792 pixels or within adjacent land pixels. Then, water frequency and multi-scene mean indexes were  
793 recalculated using the gap-filled Landsat images. Water mask classification was carried out with  
794 these recalculated indexes.

### 795 **A.2 Correction factor for observation confidence**

796 The correction factor  $f_{NDLI}$  in equation (5) was introduced to distinguish highly reflective  
797 vegetation/rock from cloud or ice/snow. The Normalized Difference Land Index (NDLI) was  
798 defined as follows:

$$799 \quad NDLI = \frac{\min[\rho_G, \rho_R] - \max[\rho_{NIR}, \rho_{SWIR}]}{\min[\rho_G, \rho_R] + \max[\rho_{NIR}, \rho_{SWIR}]} \quad (A1).$$

800 Given that vegetation and rock have relatively low reflectance in visible bands compared to  
801 infra-red bands, land shows higher NDLI than cloud and ice/snow. The correction factor  $f_{NDLI}$   
802 was calculated by equation (A2):



$$803 \quad f_{NDLI} = \begin{cases} 1 & (NDLI < 0) \\ 1 - NDLI \times 2 & (0 \leq NDLI < 0.5) \\ 0 & (0.5 \leq NDLI) \end{cases} \quad (A2).$$

804 No correction is made on the probability index  $Pci$  if  $f_{NDLI}$  equals 1, while probability of  
 805 cloud/ice existence becomes lower when  $f_{NDLI}$  is smaller.

806 The correction factor using brightness temperature  $f_{Tb}$  in equation (5) was applied to  
 807 improve the accuracy of cloud/ice detection. Given that cloud and ice/snow are relatively cold,  
 808 brightness temperature of pixels covered by cloud or ice/snow is expected to be low. The  
 809 correction function  $f_{Tb}$  was defined separately for ice/snow and cloud. Given that ice has very  
 810 low reflectivity in the short wave infra-red band, ice shows higher NDWI than cloud. We  
 811 assumed that NDWI smaller than 0.3 represents cloud. The correction function  $f_{Tb}$  was given  
 812 as follows:

$$813 \quad \begin{aligned} & \text{if } (NDWI < 0.3); \\ & f_{Tb} = \begin{cases} 1 & (Tb < 25) \\ (30 - Tb) \times 0.2 & (25 \leq Tb < 30) \\ 0 & (30 \leq Tb) \end{cases} \\ & \text{if } (NDWI \geq 0.3); \\ & f_{Tb} = \begin{cases} 1 & (Tb < 0) \\ (5 - Tb) \times 0.2 & (0 \leq Tb < 5) \\ 0 & (5 \leq Tb) \end{cases} \end{aligned} \quad (A3).$$

814 We assumed that pixels are not likely to represent cloud and ice/snow when the brightness  
 815 temperature was higher than 25 degrees centigrade and 0 degrees centigrade, respectively. No  
 816 correction was made on the probability index  $Pci$  if  $f_{Tb}$  equals 1, while probability of  
 817 cloud/ice existence becomes lower when  $f_{Tb}$  is smaller.

### 818 **A.3 Correction factor for water probability**

819 Because shadows sometimes show a high NDWI similar to water, the correlation function  
820 using NDVI  $f_{NDVI}$  was used to modify water probability in equation (6). The reflectivity of  
821 water is very low in both near infra-red and short wave infra-red bands, while the reflectivity of  
822 shadow is not as low as water in near infra-red band. Therefore, pixels with high NDWI and  
823 high NDVI are potentially affected by shadows. The correction function  $f_{NDVI}$  was given by  
824 Equation (A4):

$$825 \quad f_{NDVI} = \begin{cases} 1 & (NDVI < 0.1) \\ (0.2 - NDVI) \times 10 & (0.1 \leq NDVI \leq 0.2) \\ 0 & (0.2 < NDVI) \end{cases} \quad (A4).$$

826 No correction is made on  $P_{NDWI}$  when  $f_{NDVI}$  is 1,  $P_{NDWI}$  is reduced when  $f_{NDVI}$  is  
827 smaller than 1. As non-vegetated areas have a low NDVI, the correction function  $f_{NDVI}$  is  
828 expected to identify shadow well in vegetated areas, but may be less useful in detecting shadow  
829 in non-vegetated areas.

830